

Computational Modeling of the Driving Forces Behind Fiber-optic Distributed Magnetic Sensing

Tomas Snyder¹, Shihao Yuan¹, Eileen R. Martin¹,
Daniel Homa², Zach Dejneka², Gary Pickrell², Anbo Wang³, Logan Theis³

¹Center for Wave Phenomena, Colorado School of Mines, Golden, CO 80401

²Center for Photonics Technology, Virginia Tech, Blacksburg, VA 24061

³Sentek Instrument, LLC, Blacksburg, VA 24060

email: tsnyder1@mines.edu

ABSTRACT

Compared to standard acoustic sensing fibers that are purely sensitive to strain motions, the proposed Distributed Magnetic Sensing (DMS) fibers employ additional magnetostrictive materials embedded in the fiber cladding, making them sensitive to magnetic-field-induced strain motions. DMS offers unparalleled spatial resolution and cost-effectiveness compared to classical point-wise magnetometers, especially in challenging-to-access areas. In this study, we explore the magnetic response through theoretical modeling, the influence of temperature on DMS, and potential geophysical applications in various borehole environments. This study provides a basic understanding of the measuring principle of DMS and guidelines for ongoing and future research on improving and applying DMS to geophysical surveys.

Key words: Magnetostriction, distributed fiber optic sensing, temperature, magnetic sensing, electromagnetic modeling

1 INTRODUCTION

Distributed fiber optic sensing of static strain, dynamic strain, and temperature has become increasingly adopted for time-lapse monitoring of subsurface and well conditions. The ability to carry out long-term electric and magnetic monitoring campaigns along with geomechanical, seismic, and temperature monitoring can help us better constrain the geology and fluids in a reservoir, or can help us detect potential well integrity issues (Alambaugh et al., 2021). While distributed electric sensing is also currently being pursued simultaneously, this report focuses on understanding an in-development fiber-optic sensing technique for measuring magnetic fields called distributed magnetic sensing (DMS).

Recent advances in fiber optic production technology allow us to embed materials that respond to magnetic fields (e.g. nickel or Metglas) in single-mode fiber optics while they are being drawn. By embedding these materials in the fiber optic rather than having an external material, the nickel or Metglas material is protected from degradation, such as the corrosion that can happen in subsurface CO₂ sequestration or other scenarios. When these materials expand or contract in response to a magnetic field, a process known as magnetostriction, some of that strain is transferred to the fiber core as another source of strain that can be measured with a distributed acoustic sensing (DAS) interrogator. Subsurface magnetic sensing requires high sensitivity, so Bragg gratings are written into these specialty fibers to create discrete reflectors. Changes in the material, spacing, treatment of the material before/during the fiber draw process, and the amount of embedded material can affect the strength of the fiber response measured by the DAS interrogator (Dejneka et al., 2024; Hileman et al., 2022).

Because this technique of measuring the changes in a magnetic field with fiber optics is indirect, it is important to be able to model any non-linearities in the mechanism by which these data are acquired. This modelling capability will be essential to interpreting and inverting data from any future field trials of the new sensing system, as well as delineating any constraints on the design of reliable experiments. This report provides an overview of the magnetostriction mechanism behind the response of the embedded

materials and presents an overview of 3D simulations of magnetostriction. Specifically, we investigate the anticipated response to applied magnetic fields at varying amplitudes and frequencies, and the expected changes in response at variable temperatures. This report focuses primarily on temperature ranges that would be experienced in surface and shallow subsurface tests, but provides a path forward for higher temperature modelling that could be relevant to deeper scenarios. Further, we simulate expected responses to several borehole casing scenarios to understand the potential for identifying well integrity issues.

2 THEORY OF MAGNETOSTRICTION

Magnetostriction is the strain induced in a ferromagnetic material by an effective magnetic field, \mathbf{H}_{eff} , which includes the applied magnetic field and fields generated within the material (Cullity and Graham, 2009). Domains within ferromagnetic materials have magnetization magnitudes at the saturation magnetization value M_s . When a ferromagnetic material is in an ideal demagnetized state (i.e. all magnetic domain orientations are of the same volume), the material exhibits a net zero external magnetic field. When an external magnetic field \mathbf{H} is applied to the material, the domain magnetic moments \mathbf{M} experience a torque per volume which aligns the overall magnetic moment of the material in the direction of \mathbf{H} if $\|\mathbf{H}\|$ is large enough to saturate the material. The Landau-Lifshitz-Gilbert (LLG) equation,

$$\frac{d\mathbf{M}}{dt} = \gamma^* (\mathbf{M} \times \mathbf{H}_{eff}) - \frac{\alpha}{M} \left(\mathbf{M} \times \frac{d\mathbf{M}}{dt} \right), \quad (1)$$

describes the dynamics of the total magnetic moment of a ferromagnetic material (Gilbert, 2004; Wieser, 2015), accounting for damping of the domain motion. In eqn. 1, the constant $\gamma^* = \gamma(1 + \alpha^2)$, with $\gamma = \frac{ge}{2mc}$, where e and m are the charge and mass of the electron, c is the speed of light, and g is the spectroscopic splitting factor ($g = 2$ for electron spin); and the damping term $\alpha = \lambda/\gamma M$, where λ is an adjustable damping parameter.

In materials that exhibit magnetostriction, the cubic structure is not perfectly cubic (e.g. slightly tetragonal or rhombohedral) so the material undergoes a change in length Δl , and a subsequent strain $\lambda_s = \Delta l/l$, when the domains are reoriented. The strain experienced by an anisotropic cubic crystal when magnetized from the ideal demagnetized state to saturation in the direction defined by the direction cosines α_1, α_2 , and α_3 (representing a normalized 3D vector) and measured in the direction defined by the direction cosines β_1, β_2 , and β_3 relative to the crystal axes is

$$\lambda_s = \frac{3}{2} \lambda_{100} \left(\alpha_1^2 \beta_1^2 + \alpha_2^2 \beta_2^2 + \alpha_3^2 \beta_3^2 - \frac{1}{3} \right) + 3 \lambda_{111} (\alpha_1 \alpha_2 \beta_1 \beta_2 + \alpha_2 \alpha_3 \beta_2 \beta_3 + \alpha_3 \alpha_1 \beta_3 \beta_1), \quad (2)$$

where λ_{100} and λ_{111} are the saturation magnetostrictions in the [100] and [111] crystal directions (Cullity and Graham, 2009). Assuming the magnetostriction of the material is isotropic simplifies eqn. 2 to

$$\lambda_\theta = \frac{3}{2} \lambda_s \left(\cos^2 \theta - \frac{1}{3} \right), \quad (3)$$

where λ_s is the isotropic saturation magnetostriction and θ is the angle between the measurement direction and the saturated direction. While magnetostriction is typically not isotropic in materials, approximating the response as isotropic works well for materials with anisotropic magnetostrictions close in value, like Nickel which has saturation magnetostriction values $\lambda_{100} = -46 \text{ ppm}$, $\lambda_{111} = -24 \text{ ppm}$, and $\lambda_s = -34 \text{ ppm}$ (Hileman et al., 2022) - the negative sign indicates a decrease in length in the direction of magnetization.

3 COMPUTATIONAL MODELING

3.1 Three-dimensional magnetostriction modeling

Ubermag is an open source micromagnetic modeling package (Beg et al., 2022) that includes more complex modeling capabilities than those implemented in the two-dimensional model. In the two-dimensional model we did not specify the geometry of the material, the size of the domains, or the other fields that make up the effective field. In Ubermag, it is possible to define a three-dimensional grid of domains and run simulations from an initially demagnetized state, Figure 1. Ubermag also includes the demagnetization field, anisotropy field, exchange field, and the Zeeman (applied) field in the effective field. These fields arise in bulk materials in magnetics and are important to include because they change the dynamics of the magnetic moments and the magnetostrictive response as a result. The mathematical form of the field energies are (Beg et al., 2022):

$$w_z = -\mu_0 M_s \mathbf{m} \cdot \mathbf{H}, \quad (4)$$

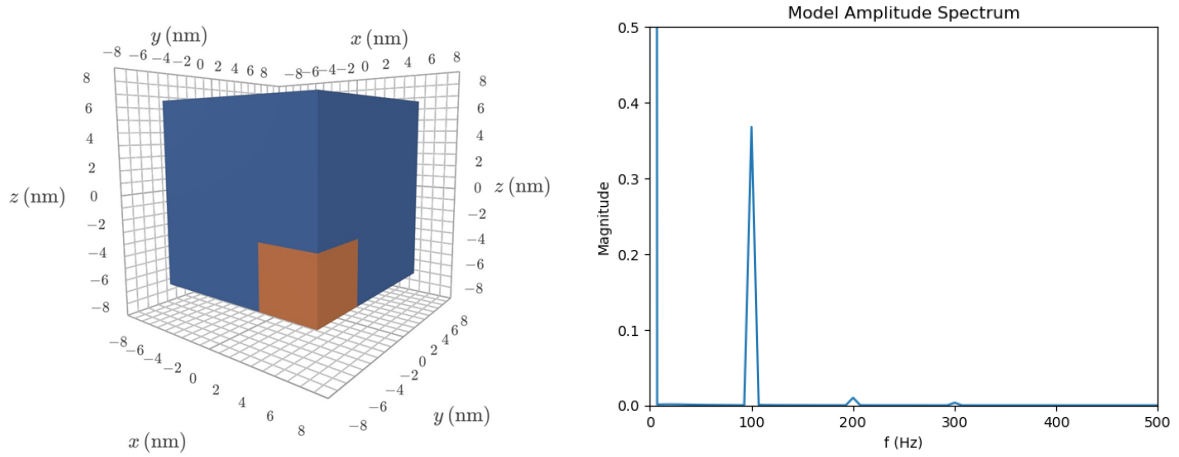


Figure 1. (left) Mesh of 3D cells defined in Ubermag. (right) 3D model results for a 100Hz source with an amplitude of 100 kA/m.

$$w_e = A(\nabla \mathbf{m})^2, \quad (5)$$

$$w_{ca} = -K_1 [(\mathbf{m} \cdot \mathbf{u}_1)^2(\mathbf{m} \cdot \mathbf{u}_2)^2 + (\mathbf{m} \cdot \mathbf{u}_2)^2(\mathbf{m} \cdot \mathbf{u}_3)^2 + (\mathbf{m} \cdot \mathbf{u}_1)^2(\mathbf{m} \cdot \mathbf{u}_3)^2], \quad (6)$$

$$w_d = \frac{1}{2} \mu_0 M_s \mathbf{m} \cdot \mathbf{H}_d. \quad (7)$$

The energies are the Zeeman energy w_z , the exchange energy w_e , the cubic anisotropy energy w_{ca} , and the demagnetization energy w_d . In addition, A is the exchange constant, K_1 is the anisotropy constant, \mathbf{H} is the external magnetic field, \mathbf{u} is the direction of the axis of anisotropy, and \mathbf{H}_d is the demagnetizing field. To solve for the effective field from the energy, we substitute the total energy E_{tot} into

$$\mathbf{H}_{eff} = -\frac{1}{\mu_0 M_s} \frac{\partial E_{tot}}{\partial \mathbf{m}}, \quad (8)$$

as in Liang et al. (2014). Substituting the result for \mathbf{H}_{eff} from eqn. 8 into eqn. 1 at each time-step allows us to solve for \mathbf{M} at each time-step. The resulting magnetic moment magnitudes are plugged into a version of eqn. 2 replacing all α_i with m_i (COMSOL, 2023),

$$\lambda_{si} = \frac{3}{2} \lambda_{100} \left(m_1^2 \beta_1^2 + m_2^2 \beta_2^2 + m_3^2 \beta_3^2 - \frac{1}{3} \right) + 3 \lambda_{111} (m_1 m_2 \beta_1 \beta_2 + m_2 m_3 \beta_2 \beta_3 + m_3 m_1 \beta_3 \beta_1), \quad (9)$$

to solve for strain, then the magnitude of the discrete fourier transform (DFT) is taken to create an amplitude spectrum of the strain response. An example amplitude spectrum is shown in Figure 1 for a source of amplitude 13 kA/m and frequency 100 Hz applied along the z -axis. There is a clear peak at the source frequency along with a double frequency peak and a small harmonic response at 300 Hz . This is a similar response to results seen in the lab, which will be discussed in the next section.

One limitation of the three-dimensional model is that the spatial scale of the cells must be smaller than the width of domain walls in the material (Abert, 2019)

$$l = \sqrt{\frac{A}{K_{eff}}}, \quad (10)$$

where A is the exchange constant and K_{eff} is the effective anisotropy constant. For Nickel, this is on the order of 10^{-7} m , meaning the cell sizes must have sides smaller than $\approx 100 \text{ nm}$. This presents an issue for modeling the fiber response since the magnetostrictive wires have diameters on the order of $10 \text{ }\mu\text{m}$ and the complexity of the 3D model increases on the order of n^2 , where n is the number of cells, due to the long range nature of the demagnetization field (Abert, 2019). Being limited to small cell sizes, modeling the actual size of the fiber may be unfeasible with this model, but modeling smaller elements may provide initial insights into the trends we expect to observe in field data. Additionally, the time-step used in the solver must be sufficiently small to satisfy the Nyquist sampling condition of two samples per period of the magnetization vector precessional motion (Scholz et al., 2003), which has a Larmor frequency of

$$\omega = \gamma \mathbf{H}_{eff}. \quad (11)$$

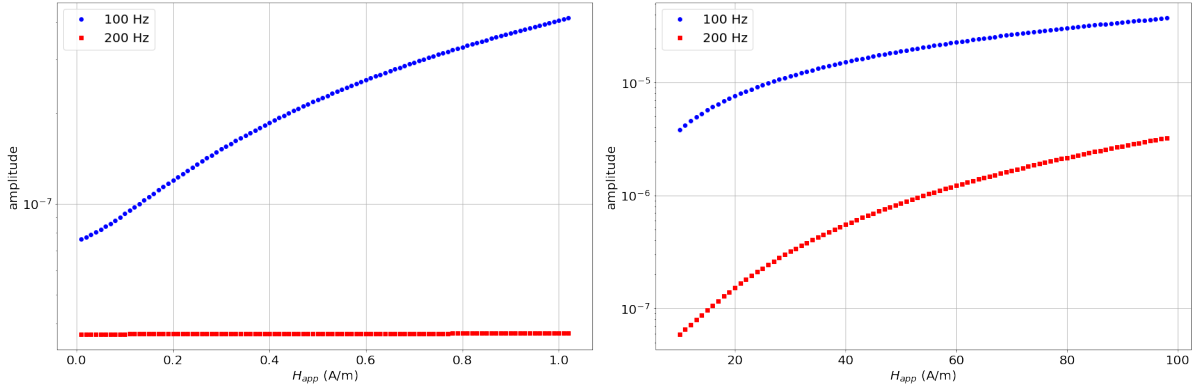


Figure 2. Plots showing the variation of the 100Hz and 200Hz peaks for (left) $0.01A/m$ to $1.02A/m$ and $10A/m$ to $98A/m$.

The magnetic field strengths tested in the lab are $2kA/m$ and lower, resulting in a Larmor frequency on the order of 5000 Hz, meaning the sampling rate must be 10000 Hz to model the physics correctly. In practice, we implement higher sampling frequencies than the Nyquist limit to ensure numerical accuracy. For lower magnetic field strengths, the sampling rate can be decreased according to the Larmor frequency.

3.2 Applied Magnetic Field Sensitivity

The amplitude spectrum of the DMS fiber varies significantly with the amplitude of the external magnetic field. To demonstrate this dependence, a suite of simulations were run from an applied magnetic field amplitude of $0.01A/m$ to $1.02A/m$ and from $10A/m$ to $98A/m$. The results of these simulations for a 100Hz source applied to Nickel, Figure 2, demonstrate how the 100Hz peak response appears at lower magnetic field than the 200Hz peak and increases predictably at higher magnetic field ranges.

The minimum magnetic field amplitude that the DMS fiber can sense in the lab is $50A/m$, which is a 100 Hz amplitude spectrum response at a 100 Hz source frequency. The 200 Hz response appears at a field strength of $400A/m$. Both of these amplitudes are higher magnetic fields than the model predicts, however, the model does predict that the 100 Hz response appears at lower magnetic fields than the 200 Hz response. The model likely is not capable of predicting the correct magnetic field strength because of a scale issue - the model is about 1000 orders of magnitude smaller than the fiber magnetic wires. Because of this scale difference, it is not possible to include the number of domains that would be present in the Nickel rods in reality. Since the domains have a magnetic field that has a lowest energy state when all domains are aligned, more domains in a system mean that the material is less susceptible to lower external magnetic fields. This is part of the reason why the model with only eight domains shows a response to lower magnetic fields than the lab experiments do.

3.3 Temperature modeling

Temperature modeling of the DMS fiber was performed using known relationships between M_s (Cullity and Graham, 2009) and α (Mankovsky et al., 2013) with temperature, Figure 3. The data from the sources cited was unavailable to us, so values for M_s were calculated for a given temperature using

$$M_s = M_0 [m - \tanh(m/t)], \quad (12)$$

where M_0 is the magnetization saturation at 0K, $m = M_s/M_0$, and $t = T/T_c$ with T_c representing the Curie temperature. The data for α as a function of temperature was fit to a Sigmoid function, resulting in the relationship for Nickel

$$\alpha(T) = 0.12677279 - \frac{0.10035642}{(1 + e^{-0.0851499(T-69.35616788)})}. \quad (13)$$

Figure 4 shows the plots resulting from equations 12 and 13. Comparing to Figure 3, we see that these functions approximate the data reasonably well. The amplitudes of the first two peaks of the amplitude spectrum produced by the temperature model for Nickel at an applied magnetic field amplitude of $H = 10kA/m$ and frequency $f = 100Hz$ is shown in Figure 5. There is not a significant amount of variation in the amplitude spectrum over the temperature range tested, which suggests that the signal does not show high dependence on temperature fluctuations for this temperature range.

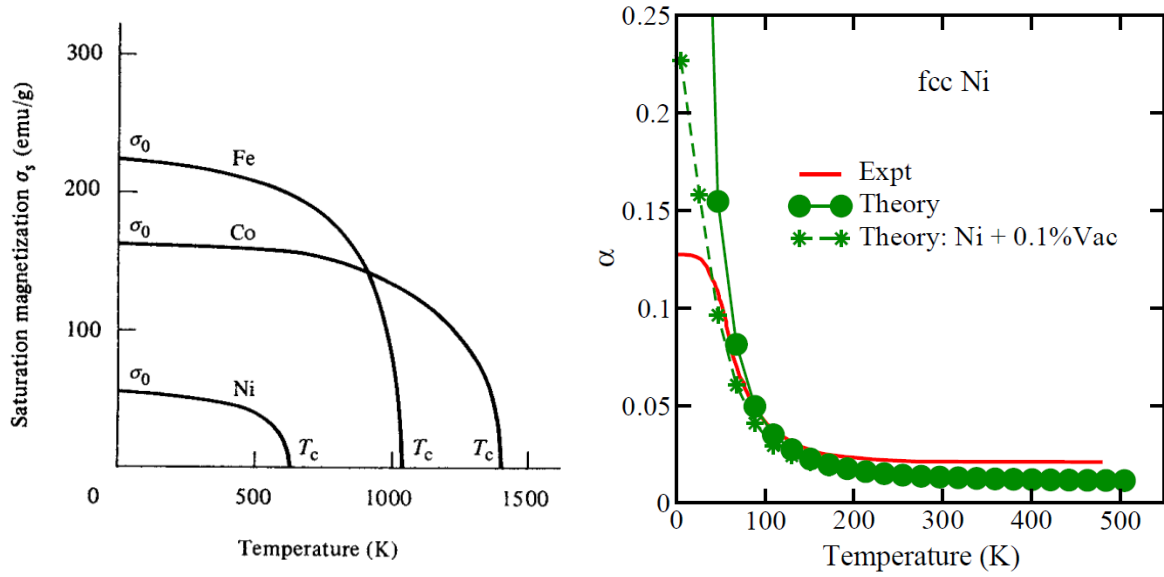


Figure 3. Plots showing the (left) relationship between temperature and M_s (Cullity and Graham, 2009) (right) and temperature and α (Mankovsky et al., 2013).

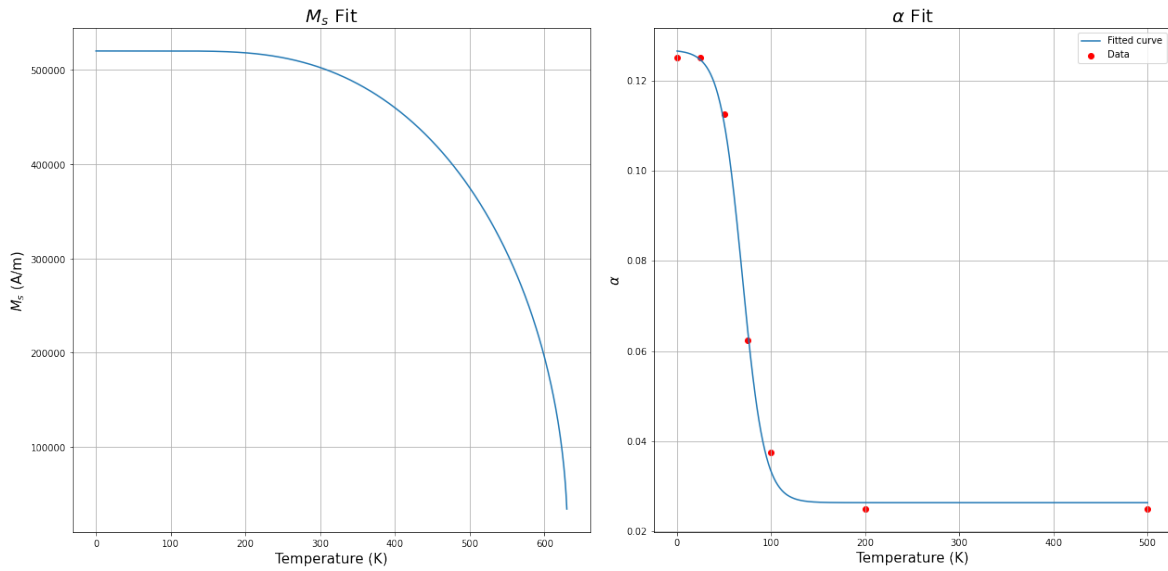


Figure 4. The modeled relationship between (left) M_s and temperature and (right) α and temperature.

3.4 Numerical modeling of magnetic sensing fiber in borehole environments

In the following, we present a series of numerical examples that assume: (1) the measured magnetic-field-induced strain along the fiber can be accurately converted to the magnetic flux density along a certain direction; (2) the magnetic optic fiber is attached to the inner casing surface, and the magnetic dipole sources are placed in the center of the well, without being attached to the casing surface. We explore the response of the magnetic fiber along a vertical borehole under three scenarios: (1) with and without conductive and magnetic permeable borehole casing; (2) with and without resistive oil layers surrounding the formations; (3) casing with and without gaps. We are using the open-source SimPEG (Cockett et al., 2015) software to conduct frequency-domain borehole electromagnetic (EM) simulations. The cylindrical meshes implemented in SimPEG can accurately handle the complex geometry and properties of casings, facilitating the study of casing effects in various configurations. With the 2D cylindrically symmetric

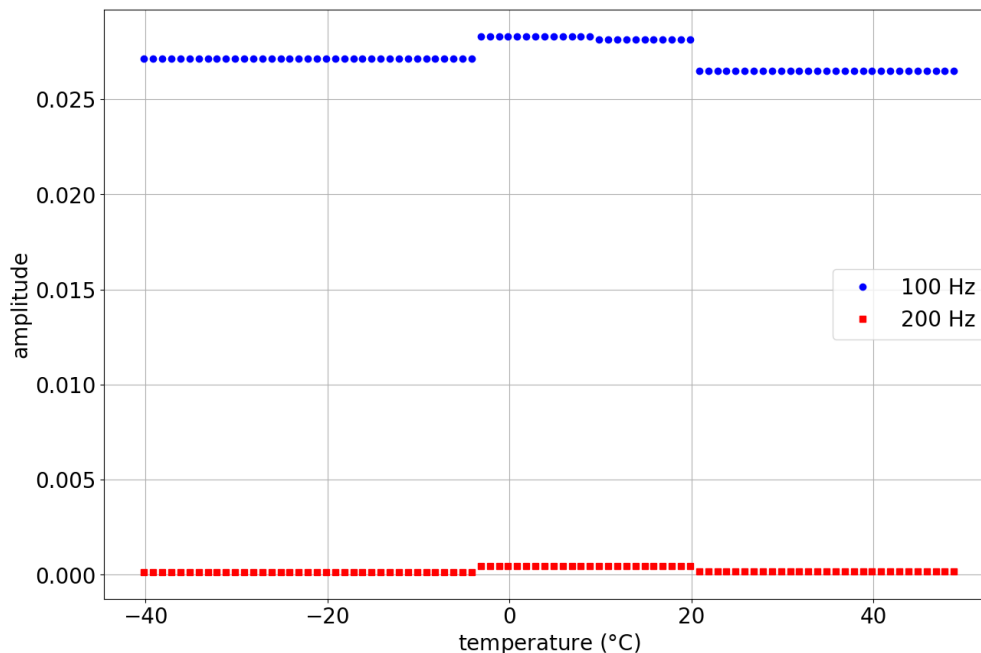


Figure 5. The amplitudes of the 100Hz and 200Hz peak for simulations at different temperatures.

meshes, we can simulate a vertically steel-cased well at a small computational cost (approximately 3 seconds per modeling run), enabling us to rapidly study the potential EM field under various borehole environments.

The first experiment compares the magnetic response in a uniform half-space with and without a vertical steel casing (Figure 6). The steel casing has a conductivity of $5 \times 10^6 S/m$, while the background conductivity is $1 \times 10^{-2} S/m$. The casing has an outer diameter of 0.1 m and a thickness of 0.01 m. The relative magnetic permeability μ_r of the casing is 100. We fix the electromagnetic (EM) source position at a depth of 1000 m, and the magnetic fiber position extends from the surface down to a depth of 2000 m. The EM source is a vertical magnetic dipole with a moment strength of $10^6 A/m^2$, generating monochromatic EM signals at a frequency of 100 Hz. Top panel of Figure 7 describes the conductivity models, and the bottom panel shows the magnetic field on the inner surface of the casing. Since the casing behaves like a waveguide, the magnetic flux density (represented by the cyan line) decays much slower vertically with the casing than without the casing (represented by the black line in the bottom panel of Figure 7).

One interesting aspect during oil production or CO_2 injection is how the oil-water ratio or CO_2 saturation change along the well. Since oil and CO_2 are more electrically resistive than water, we examine the sensitivity of the magnetic field along the magnetic sensing fiber to changes in the electrical properties along the well. We add two resistive layers to the background model (Top panel of Figure 8) as the monitoring model. The bottom panel of Figure 8 shows the magnetic flux density under the background and monitoring models, as well as their differential magnetic field. The source and fiber geometry are the same as in the previous experiment.

Well casings are designed to prevent fluids from different formations from mixing during production or injection operations. Gaps or cracks in the casing can lead to potential cross-flow of fluids between formations, compromising well integrity and potentially causing leaks. Detecting and monitoring these casing gaps is crucial for maintaining well integrity. In the next example, we consider a monitoring model with two gaps introduced in the casing (Figure 9). As shown in the bottom panel of Figure 9, the maximum differential magnetic field directly indicates the location of the casing gaps. By leveraging the sensitivity of EM signals to changes in electrical conductivity and magnetic permeability, EM methods have the potential to detect and locate casing gaps or leaks without requiring direct access to the well.

4 CONCLUSIONS

Distributed magnetic sensing technologies are being developed to enable continuous monitoring of surface and subsurface processes, but the magnetostriction mechanism that enables their response is governed by a nonlinear equation. Three-dimensional

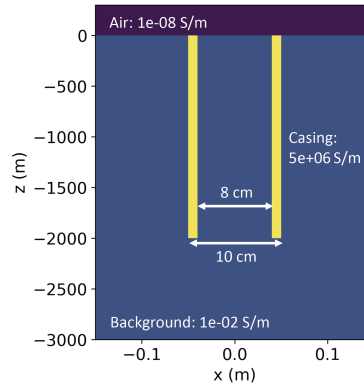


Figure 6. Casing geometry. The steel casing has a conductivity of $5 \times 10^6 \text{ S/m}$, while the background conductivity is $1 \times 10^{-2} \text{ S/m}$. The casing has an outer diameter of 0.1 m and a thickness of 0.01 m.

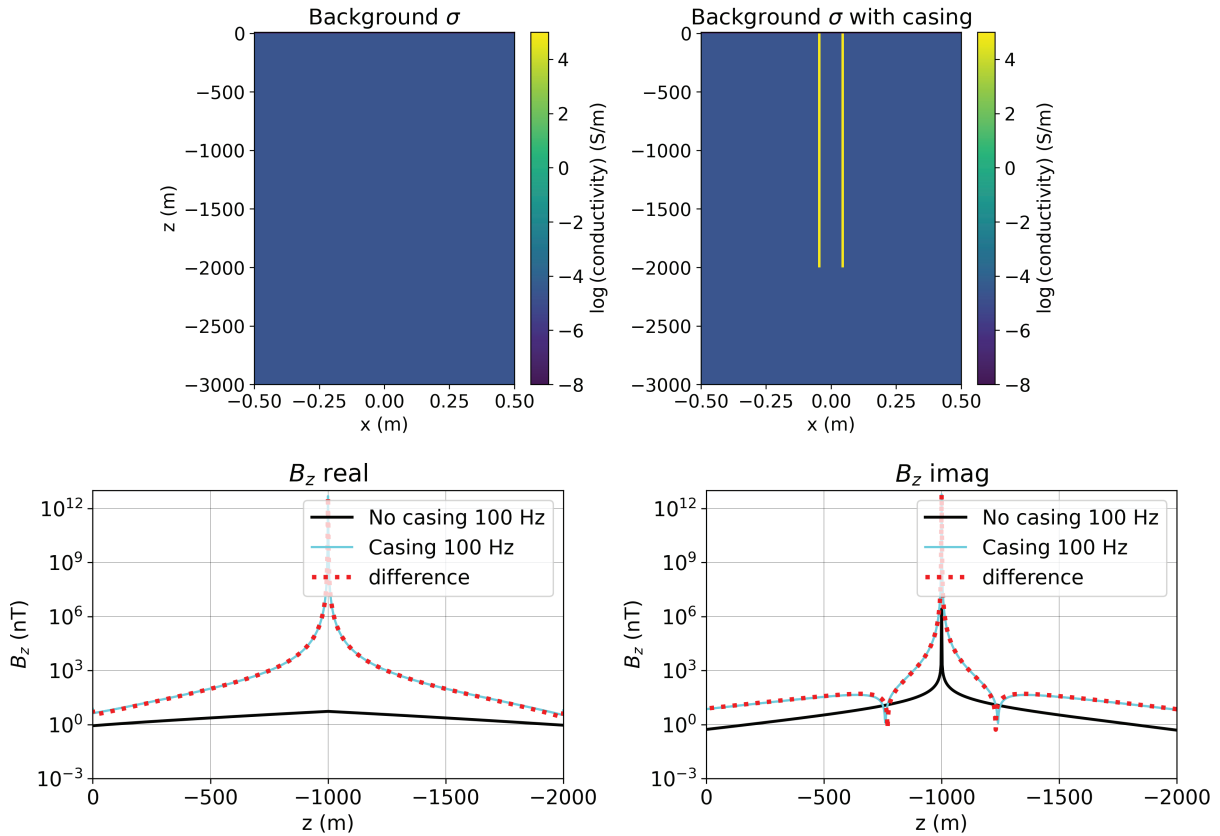


Figure 7. Top: Conductivity of the borehole model with and without steel casing. Bottom: Time-lapse vertical magnetic flux density on the inner surface of the steel-cased well.

numerical simulations have enabled us to better model the responses of fibers tested in laboratory settings, but precise results do rely on several calibrations or material property assumptions. These simulations can be used to predict the amplitude response to varying magnetic field sources, but further scalability studies are needed for more realistic large-scale simulations. The magnetostrictive response does vary with temperature, but our simulations of this response change shows that the variation is relatively small for typical surface and shallow subsurface conditions (i.e. between -40 C and 50 C), suggesting that this can be optionally included as a secondary effect in analyzing future field data within these temperature ranges. We consider the potential future appli-

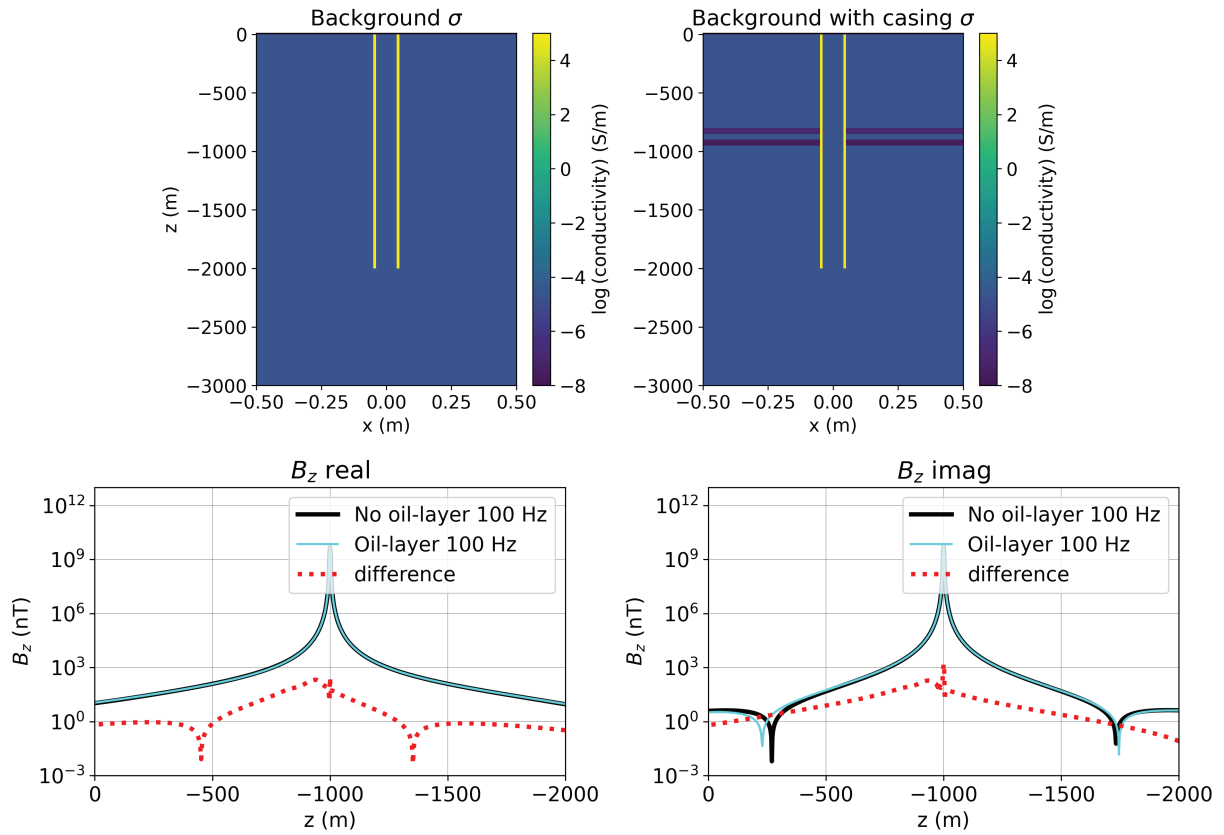


Figure 8. Top: Conductivity of the borehole model with and without two resistive oil layers. Bottom: Time-lapse vertical magnetic flux density on the inner surface of the steel-cased well.

cation of well casing integrity evaluation, both with and without fluid layers in the formation, and with and without casing or gaps in casing. These studies suggest that applications in well integrity monitoring are a likely use case for these distributed magnetic sensing fibers.

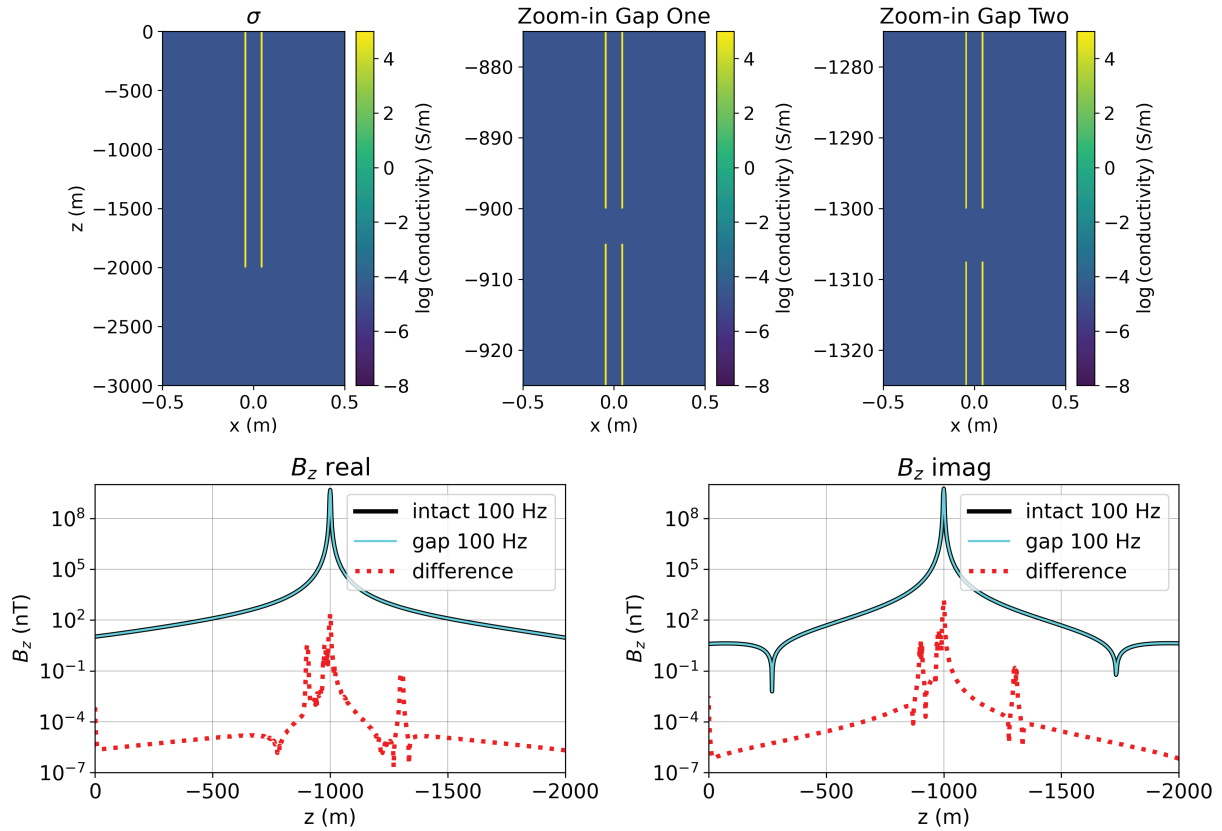


Figure 9. Top: Conductivity of the borehole model with and without casing gaps. Bottom: Time-lapse vertical magnetic flux density on the inner surface of the steel-cased well.

5 ACKNOWLEDGEMENTS

We thank the sponsor companies of the Center for Wave Phenomena, and Department of Energy SBIR contract DE-SC0023984 with Sentek, whose support made this research possible.

REFERENCES

- Abert, C., 2019, Micromagnetics and spintronics: models and numerical methods: *The European Physical Journal B*, **92**.
- Alambaugh, D., E. Um, G. Hoversten, and K. Key, 2021, Distributed electric field sensing using fibre optics in borehole environments: *Geophysical Prospecting*, **70**, 210–221.
- Beg, M., M. Lang, and H. Fangohr, 2022, Ubermag: Towards more effective micromagnetic workflows: *IEEE Transactions on Magnetics*, **58**, 1–5.
- Cockett, R., S. Kang, L. J. Heagy, A. Pidlisecky, and D. W. Oldenburg, 2015, Simpeg: An open source framework for simulation and gradient based parameter estimation in geophysical applications: *Computers & Geosciences*, **85**, 142–154.
- COMSOL, 2023, Magnetostrictive material: COMSOL Documentation.
- Cullity, B., and C. Graham, 2009, *Introduction to magnetic materials*, 2 ed.: John Wiley & Sons, Inc.
- Dejneka, Z., D. Homa, J. Buontempo, G. Crawford, E. Martin, L. Theis, A. Wang, and G. Pickrell, 2024, Magnetic field sensing via acoustic sensing fiber with metglas 2605sc cladding wires: *Photonics*, **11**, 348.
- Gilbert, T. L., 2004, A phenomenological theory of damping in ferromagnetic materials: *IEEE Transactions on Magnetics*, **40**, 3443–3449.
- Hileman, Z., D. Homa, L. Ma, B. Dong, E. Martin, G. Pickrell, and A. Wang, 2022, Development of a multimaterial optical fiber for fully distributed magnetic sensing applications: *IEEE Sensors Letters*, **6**, 1–4.

- Liang, C.-Y., S. M. Keller, A. E. Sepulveda, A. Bur, W.-Y. Sun, K. Wetzlar, and G. P. Carman, 2014, Modeling of magnetoelastic nanostructures with a fully coupled mechanical-micromagnetic model: *Nanotechnology*, **25**, 435701.
- Mankovsky, S., D. Koedderitzsch, G. Woltersdorf, and H. Ebert, 2013, First-principles calculation of the gilbert damping parameter via the linear response formalism with application to magnetic transition-metals and alloys: *Physical Review B*, **87**.
- Scholz, W., J. Fidler, T. Schrefl, D. Suess, R. Dittrich, H. Forster, and V. Tsiantos, 2003, Scalable parallel micromagnetic solvers for magnetic nanostructures: *Computational Materials Science*, **28**, 366–383. (Proceedings of the Symposium on Software Development for Process and Materials Design).
- Wieser, R., 2015, Description of a dissipative quantum spin dynamics with a landau-lifshitz/gilbert like damping and complete derivation of the classical landau-lifshitz equation: *The European Physical Journal B*, **88**.